Influence of Alumina Type on the Evolution and Activity of Alumina-Supported Fe Catalysts in Single-Walled Carbon Nanotube Carpet Growth

Placidus B. Amama,[†,‡,*] Cary L. Pint,[§] Seung Min Kim,[⊥] Laura McJilton,[§] Kurt G. Eyink,[†] Eric A. Stach,[⊥] Robert H. Hauge,[§] and Benji Maruyama[†,*]

[†]Air Force Research Laboratory, Materials and Manufacturing Directorate, Wright-Patterson Air Force Base, Ohio 45433, [‡]University of Dayton Research Institute (UDRI), University of Dayton, Dayton, Ohio 45469, [§]Department of Physics, Department of Chemistry, and Richard E. Smalley Institute for Nanoscale Science and Technology, Rice University, Houston, Texas 77251, and [⊥]School of Materials Engineering, and Birck Nanotechnology Center, Purdue University, West Lafayette, Indiana 47907

ABSTRACT We have studied the lifetime, activity, and evolution of Fe catalysts supported on different types of alumina: (a) sputter deposited alumina films (sputtered/Fe), (b) electron-beam deposited alumina films (e-beam/Fe), (c) annealed e-beam deposited alumina films (annealed e-beam/Fe), (d) alumina films deposited by atomic layer deposition (ALD/Fe), and (e) c-cut sapphire (sapphire/Fe). We show that the catalytic behavior, Ostwald ripening, and subsurface diffusion rates of Fe catalyst supported on alumina during water-assisted growth or "supergrowth" of single-walled carbon nanotube (SWNT) carpets are strongly influenced by the porosity of the alumina support. The catalytic activity increases in the following order: sapphire/Fe < annealed e-beam/Fe < ALD/Fe < e-beam/Fe < sputtered/Fe. With a combination of microscopic and spectroscopic characterization, we further show that the Ostwald ripening rates of the catalysts and the porosity of the alumina support correlate with the lifetime and activity of the catalysts. Specifically, our results reveal that SWNT carpet growth is maximized by very low Ostwald ripening rates, mild subsurface diffusion rates, and high porosity, which is best achieved in the sputtered/Fe catalyst. These results not only emphasize the connection between catalytic activity and particle stability during growth, but guide current efforts aimed at rational design of catalysts for enhanced and controlled SWNT carpet growth.

KEYWORDS: Fe catalyst · alumina support · carbon nanotube carpets · catalyst lifetime · catalyst activity · porosity · ellipsometry

There has been growing interest in densely packed, vertically aligned single-walled carbon nanotube (SWNT) carpets because of their suitability in several important applications such as, supercapacitors,[1] self-cleaning "gecko" adhesives,[2] nanofiltration membranes,[3] polymer−nanotube composites,[4] and electrodes for lithium-ion batteries.[5] Among the existing methods for the growth of carbon nanotubes (CNTs), catalyst-assisted chemical vapor deposition (CVD) appears to be the most suitable for SWNT carpet growth.[6−9] The catalyst commonly used for SWNT carpet growth is a thin Fe film (<1 nm thick) supported on an alumina film with thickness in the range of 10−200 nm.[6−9] Using this catalyst and a hydrocarbon feedstock, highly dense SWNT carpets of millimeter-scale heights can be achieved *via* the water-assisted CVD growth (or "supergrowth") process advanced by Hata *et al.*[6] Although the lifetime and activity of the alumina−Fe catalyst is enhanced by the supergrowth process, growth termination of the SWNT carpets still limits yield. Therefore, to fully achieve the promise of SWNT carpets, a rational approach for the design of catalysts with longer lifetime and higher activity is required.

Like other catalytic reactions, the growth of CNTs by CVD is extremely sensitive to the nature of the catalyst support.[10,11] For instance, while alumina is a good support for SWNT carpet growth from Fe catalyst as shown by the increased CNT nucleation density, other oxides used for CNT growth such as SiO_2, TiO_2, TiN, and ZrO_2 do not appear to support aligned growth.[12−14] A characteristic feature of alumina is that it is able to restrict the surface mobility of Fe because of a stronger substrate−catalyst interaction.[12,15,16] Similar stabilization effect induced by the substrate−catalyst interaction has been observed in other catalysts used for the controlled growth of SWNTs such as Co-MCM-41; the stabilization mechanism in this case is hypothesized to consist of the incorporation of Co^{2+} ions in the silica rings that form the MCM-41 structure.[17,18]

Recently, we showed that mass loss due to Ostwald ripening[19] and atomistic subsurface diffusion[20] of the catalyst during carpet growth are intrinsically linked to

*Address correspondence to Benji.Maruyama@wpafb.af.mil, Placidus.Amama@wpafb.af.mil.

Received for review November 25, 2009 and accepted January 18, 2010.

Published online February 4, 2010. 10.1021/nn901700u

the growth termination process. Since these phenomena depend in part on the nature of the catalyst support, the results of these studies further reinforce the critical role played by the support layer. The Fe−alumina catalytic system has been used successfully in hydrocarbon reforming, Fischer−Tropsch, and ammonia synthesis reactions, and the important role alumina plays as a structural modifier has been well documented.[21] However, there still remain many important areas of Fe−alumina catalytic system not addressed, especially in the context of SWNT carpet growth. This includes how the type of alumina (based on deposition method) and the porosity affect the evolution, activity, and lifetime of the catalyst. This study is a critical step toward establishing a rational basis for the design of catalysts with high or infinite lifetime for SWNT carpet growth. It is important to note that each type of alumina used as a support has its distinct material properties (density, porosity, roughness, and surface energy), and these properties can influence the catalyst evolution, and ultimately SWNT carpet properties.

In the present work, we demonstrate that under SWNT carpet growth conditions there is a strong connection between catalytic activity and particle stability. Our results reveal remarkable differences in the activity and lifetime of Fe catalyst supported on different types of alumina (c-cut sapphire and thin alumina films deposited by different methods). These observed differences in their catalytic behavior have been investigated further in the context of Ostwald ripening, atomistic subsurface diffusion, and porosity of the alumina supports using a combination of microscopic and spectroscopic characterization.

RESULTS AND DISCUSSION

The effect of the alumina type on the activity and lifetime of the catalyst was studied by performing SWNT carpet growth on the different alumina-supported catalyst samples using water-assisted growth conditions.[22] The following catalysts were studied: (a) Fe supported on sapphire (sapphire/Fe), (b) Fe supported on sputter-deposited alumina (sputtered/Fe), (c) Fe supported on electron-beam deposited alumina (e-beam/Fe), (d) Fe supported on thermally annealed alumina deposited by e-beam (annealed e-beam/Fe), and (e) Fe supported on alumina deposited by atomic layer deposition (ALD/Fe). The estimation of the activity and lifetime of the catalysts is based on the measured carpet height. The results of carpet height are based on average of 5−7 height measurements taken *via* field emission scanning electron microscopy (FESEM) on the side of the carpet (Supporting Information, SI 1). The presence of radial breathing modes (RBMs) in the Raman spectra of the carpets (Supporting Information, SI 2) verifies that these carpets are composed of SWNTs. The "catalytic activity" as used herein refers to the increase in the SWNT carpet height with time while the "catalyst lifetime", also deduced from the carpet height, refers to the time after which the catalyst has basically lost its catalytic function to grow SWNT carpets. As presented in Figure 1, there is a strong dependence of the SWNT carpet height or the catalyst lifetime on the type of alumina used as catalyst support. Sputtered/Fe appears to support a faster early growth rate and shows the longest catalyst lifetime, followed by e-beam/Fe, while annealed e-beam/Fe initially had the same rate as e-beam/Fe, but exhibits early growth termination. ALD/Fe grows SWNT carpets reasonably well, but at a slower rate and growth seems to terminate shortly after 15 min. FESEM characterization of carpets grown on ALD/Fe (Supporting Information, SI 3) confirms that growth termination is associated with the distinct loss of alignment among the SWNTs as shown by Hart *et al.*[23,24] Surprisingly, sapphire/Fe does not support carpet or aligned vertical growth at all. Although long catalyst lifetime in the growth of ultralong nanotubes up to 4.7 mm has been attributed to the dense Al_2O_3 buffer layer,[25] we did not observe the same phenomenon in the annealed e-beam/Fe, a system that is known to be denser than the other deposited layers studied. It is worth pointing out that pristine alumina films (without Fe) were exposed to SWNT carpet growth conditions and we observed no formation of CNTs or pyrolized carbon, suggesting that the alumina support in itself is catalytically inactive.

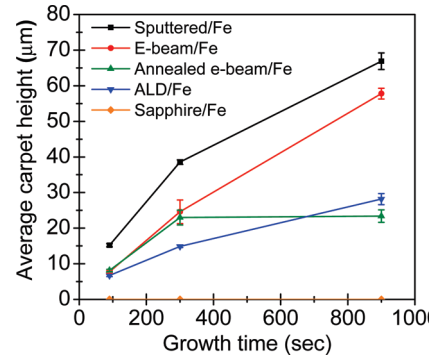

Figure 1. Plots showing average SWNT carpet height as a function of growth time for sputtered/Fe, e-beam/Fe, annealed e-beam/Fe, ALD/Fe, and sapphire/Fe. The results of carpet height are based on 5−7 height measurements taken *via* FESEM on the side of the carpet. There is a strong dependence of the average carpet height on the type of alumina used as catalyst support.

To gain insights into the observed differences in the catalyst activity and lifetime, we carried out a time-dependent study whereby the different alumina-supported Fe catalysts were exposed to carpet growth environment in the presence and absence of C_2H_2. Studies performed in the absence of the carbon feedstock allowed for better catalyst size analysis and thus proper isolation of the ripening phenomenon. The reliability of this approach was confirmed previously, as the ripening trend of the catalyst is the same regardless of

the presence or absence of C_2H_2.[19] It is well-known that when catalyst films are subjected to thermal treatment, the mobility of metal atoms increases, resulting in Ostwald ripening[26]—a phenomenon that is driven by the lowering of the surface free energy of the catalyst nanoparticles relative to the bulk. Representative tapping-mode AFM data of the as-deposited 0.5 nm-thick Fe films supported on the different types of alumina, and Fe_2O_3 nanoparticles formed on the alumina supports after exposure to SWNT carpet growth conditions in the absence of C_2H_2 for 1.5 and 5 min are presented in Figure 2. A summary of the catalyst properties after thermal treatment are also presented in Table 1. Severe ripening is observed for sapphire/Fe followed by annealed e-beam/Fe and ALD/Fe after 5 min while e-beam/Fe and sputtered/Fe remain relatively stable.

The AFM images of the as-deposited alumina/Fe samples in Figure 2a,d,g,j,m reveal striking differences in the wetting behavior of Fe on the various alumina. The as-deposited sputtered/Fe, e-beam/Fe, and ALD/Fe samples had preformed catalyst nanoparticles (<3 nm in mean height) on the surface while the as-deposited annealed e-beam/Fe and sapphire/Fe samples had a somewhat continuous and smoother film in which discrete particles were not discernible. This observation is also supported by cross-sectional TEM data (not shown) and the variation in the average surface roughness. The average surface roughness increases in the order: sapphire/Fe (0.15) < annealed e-beam/Fe (0.19) < e-beam/Fe (0.21) < ALD/Fe (0.23) < sputtered/Fe (0.26). Because of the higher surface energy of Fe than alumina, it is expected that Fe will form islands on the support. The different wetting behavior observed may be due to differences in their surface energies (*i.e.*, their surface defect densities, surface roughness, and film density). The high density of the α-alumina film enhances the uniformity of the Fe film upon deposition.[27] Thus, the improved wettability of Fe on sapphire and annealed e-beam/Fe may be due to their higher density and surface energy. Note that for annealed e-beam/Fe, the annealing of the original e-beam deposited alumina film increases the density and transforms the amorphous film to polycrystalline alumina. On the other hand, it is probable that sputtered/Fe, e-beam/Fe, and ALD/Fe have amorphous alumina films with surface energies that may impede the wetting of Fe and favor the formation of hemispherical Fe particles, if Fe is deposited from the gas phase.[28]

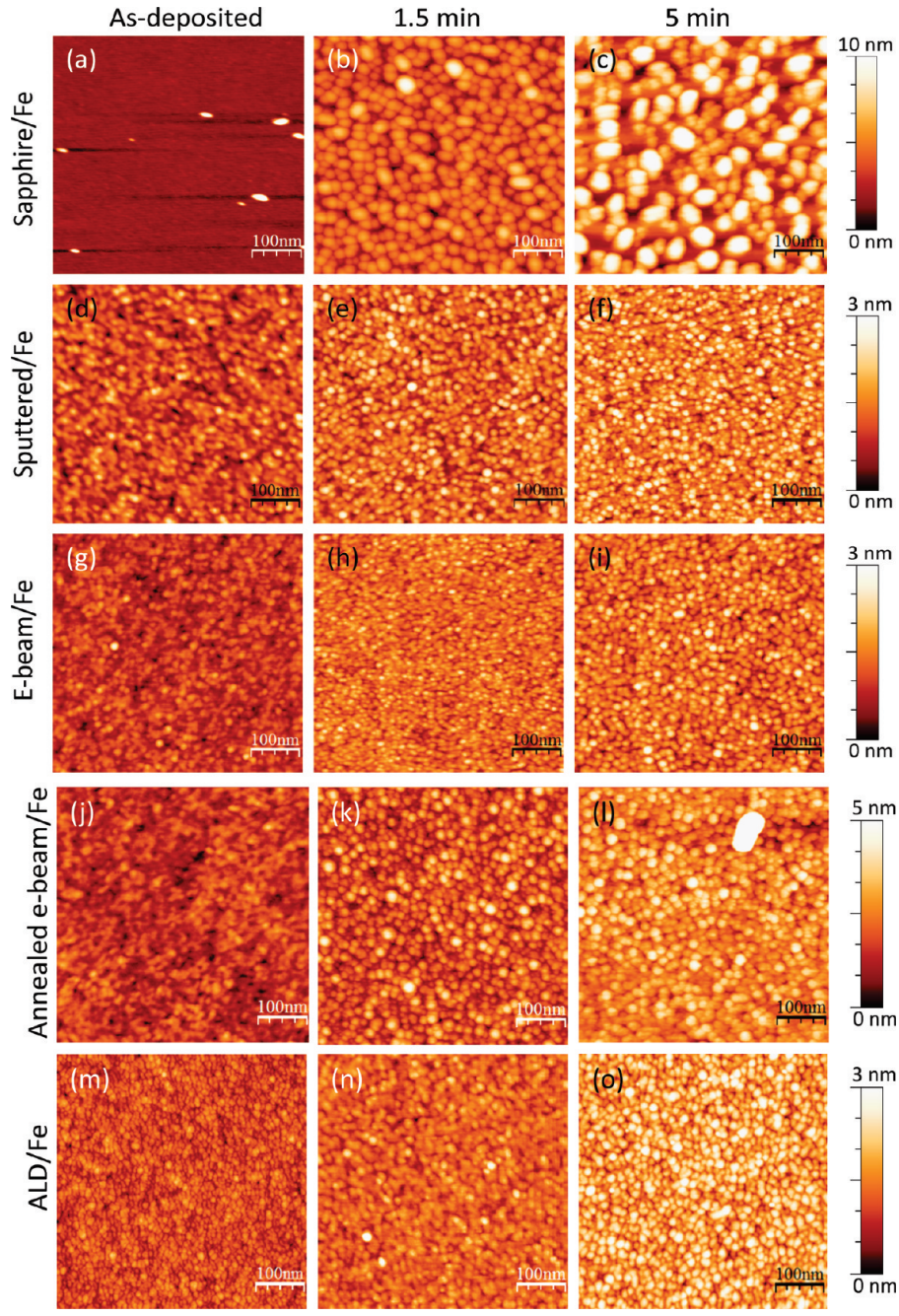

Figure 2. Catalyst evolution: AFM topography images of as-deposited catalyst and catalyst nanoparticles formed on different alumina supports after exposure to growth conditions in the absence of C_2H_2 for 1.5 and 5 min: sapphire/Fe (a−c), sputtered/Fe (d−f), e-beam/Fe (g−i), annealed e-beam/Fe (j−l), and ALD/Fe (m−o). Z-scale is 10 nm (a−c), 3 nm (d−j), 5 nm (k and l) and 3 nm (m−o). All scale bars are 100 nm.

TABLE 1. Summary of the Physical Properties of the Different Alumina-Supported Fe Catalysts after Exposure to Growth Conditions for 1.5 and 5 min in the Absence of C_2H_2 obtained from AFM

catalyst	annealing time (min)	catalyst mean height (nm)	std. dev.	catalyst number density (200 × 200 nm^2)	average surface roughness (nm)
sapphire/Fe	0				0.15
	1.5	3.60	1.12	85	0.86
	5	5.17	2.36	28	1.69
sputtered/Fe	0				0.26
	1.5	1.17	0.42	178	0.33
	5	1.45	0.41	164	0.36
e-beam/Fe	0				0.21
	1.5	1.10	0.27	209	0.21
	5	1.18	0.33	164	0.36
annealed e-beam/Fe	0				0.19
	1.5	2.07	0.68	110	0.50
	5	2.31	0.58	87	0.57
ALD/Fe	0				0.23
	1.5	0.95	0.26	138	0.24
	5	1.45	0.41	112	0.37

It is well-known that surface modification of a material has a significant effect on the surface topography.[29,30] Studies involving nanospheres of polypropylene and structural carbon fibers modified with titanium carbide revealed that their surface profiles are dependent on feature height.[30] The surface roughness increases with feature height.[29,30] This approach was also used to analyze the particle height distributions. Analysis was performed using the WXsM software.[31] The roughness analysis basically calculates the relative height of each pixel in the image and presents the data as a histogram. The resulting histograms are presented in the Supporting Information (SI 3) and the surface profiles are consistent with the observed trend in Figure 3. Since the particles on the as-deposited samples were not easily discernible, it was difficult to perform manual cross-sectional analysis. Using this method, we were able to compare the surface roughness of the as-deposited samples with those thermally annealed for 1.5 and 5 min (Table 1) to get a more complete picture

The histograms of the catalyst particle height distributions adapted from the AFM data in Figure 2 are presented in Figure 3a−e; the z-heights and number density of the particles in a 200 × 200 nm area were obtained by manual cross-sectional analysis. As shown in Table 1, the number density decreases with time, which is one of the attributes of Ostwald ripening. Another attribute of Ostwald ripening is the growth of larger particles at the expense of smaller ones to relieve the excess surface energy. A summary of the mean heights and standard deviations obtained by manual cross-sectional analysis of 50 particles randomly picked in a 200 × 200 nm^2 area are presented in Table 1. This analysis was limited to the catalyst evolution between 1.5 and 5 min due to the absence of easily resolved particles in the as-deposited samples, which made manual analysis of their AFM images difficult. Figure 3 confirms that there is severe coarsening of the catalyst nanoparticles especially in the case of sapphire/Fe, ALD/Fe, and annealed e-beam/Fe, evidenced by both (1) an increase in the mean height, and (2) the simultaneous disappearance of small particles (<1 nm) and the appearance of large particles (>3.5 nm for annealed/Fe and >6 nm for sapphire/Fe). On the basis of the increase in the heights of the particles presented in Figure 3, the Ostwald ripening rate seems to be highest in sapphire/Fe, intermediate in annealed/Fe and ALD/Fe, and lowest in sputtered/Fe and e-beam/Fe.

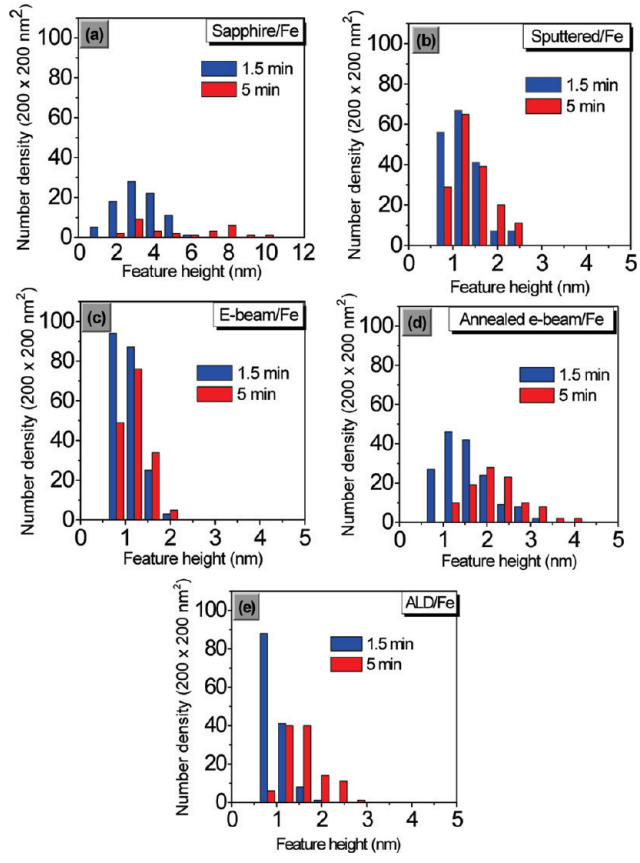

Figure 3. Histograms of feature height distributions measured from the AFM data in Figure 2 by manual cross-sectional analysis: (a) sapphire/Fe, (b) sputtered/Fe, (c) e-beam/Fe, (d) annealed e-beam/Fe, and (e) ALD/Fe in a 200 × 200 nm^2 area. Ostwald ripening rate is highest in sapphire/Fe, intermediate in annealed e-beam/Fe and ALD/Fe, and least in sputtered/Fe and e-beam/Fe.

of their ripening behavior. The surface roughness for the different samples reveals a trend that is consistent with that obtained from cross-sectional analysis (Figure 3).

The exposed catalyst layers of the samples after SWNT carpet growth for 1.5 and 5 min were also studied by AFM to further confirm the Ostwald ripening behavior observed in the absence of C_2H_2. While the same Ostwald ripening trend discussed so far is apparent in the AFM images (Figure 4), the ripening behavior of annealed e-beam/Fe and ALD/Fe samples appear distinguishable. The ripening rate appears to decrease in the following order: sapphire/Fe > annealed e-beam/Fe > ALD/Fe > sputtered/Fe ≈ e-beam/Fe. Interestingly, the ripening behavior correlates with the growth data in Figure 1, where sapphire/Fe does not support growth at all, annealed e-beam/Fe results in early growth termination, and ALD/Fe exhibits a slow growth rate. On the other hand, sputtered/Fe and e-beam/Fe both exhibit high catalytic activity and lifetime. We have shown that Ostwald ripening and subsurface diffusion of the catalysts results in the termination of SWNT growth.[19,20] We hypothesize that the reduced ripening observed for e-beam/Fe and sputtered/Fe is one of the reasons for their high catalytic activity and longer lifetime.

Raman spectroscopy is widely used for evaluating the quality of SWNTs based on the ratio of the tangential G-band occurring ~1591 cm^{-1} for SWNTs and the defect-induced D-band occurring ~1312 cm^{-1} (G/D). A summary of the G/D ratios for the growth products obtained after 1.5, 5, and 15 min from the different alumina-supported catalysts is presented in Table 2. Interestingly, the quality of CNTs obtained follows the general trend of Ostwald ripening observed and decreases in the following order: sputtered/Fe > e-beam/Fe > ALD/Fe ≈ annealed e-beam/Fe > sapphire/Fe. Therefore, the increased D-band observed for samples that do not grow carpets well is due to the formation of amorphous carbon or defects, which is most likely induced by the increased rate of Ostwald ripening.

We have previously observed that surface-mediated Ostwald ripening is dominant in the first 5 min of SWNT carpet growth while atomistic subsurface diffusion of Fe into the alumina support strongly influences in the later stage of growth.[20] Having discussed what happens in the first 5 min of growth, the focus of our discussion shifts to how the catalysts evolve on the different types of alumina after 15 min as observed by AFM, TEM, and XPS sputter depth profile analysis. Plan-view TEM images of the particles formed on the substrates after thermal annealing in the absence of C_2H_2 for 15 min (Figure 5) reveal the presence of small particles and a higher number density of particles for e-beam/Fe

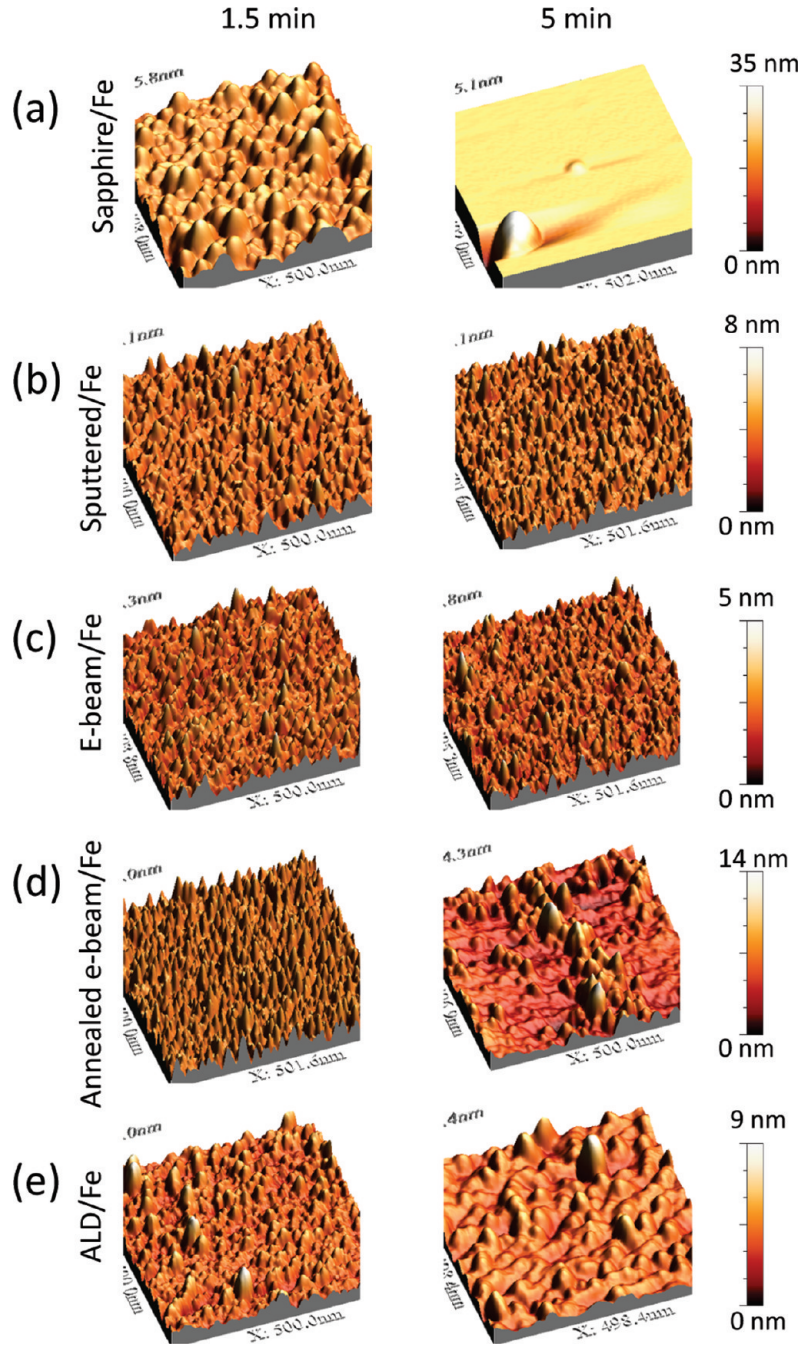

Figure 4. AFM topography images of the exposed catalyst layer after carpet growth for 1.5 and 5 min: (a) sapphire/Fe, (b) sputtered/Fe, (c) e-beam/Fe, (d) annealed e-beam/Fe, and (e) ALD/Fe. Z-scale is 35 nm (a), 8 nm (b), 5 nm (c), 14 nm (d), and 9 nm (e). Panel size: ~500 × 500 nm^2. The SWNT carpets were removed by O_2 etch at 600 °C in air for 3 min and lift-off using a clear tape. The evolution of the catalysts under SWNT carpet growth conditions is consistent with that observed in the absence of C_2H_2.

TABLE 2. Summary of the Ratio of the Intensity of the G-band to the D-band (G/D) for the Carbon Products Obtained from the Different Alumina-Supported Fe Catalysts after Exposure to Growth Conditions for 1.5, 5, and 15 min[a]

catalyst	G/D (1.5 min)	G/D (5 min)	G/D (15 min)
ALD/Fe	9.89	13.32	12.02
sputtered/Fe	22.0	28.88	29.17
e-beam/Fe	13.63	18.29	20.0
annealed/Fe	13.5	13.23	13.78
sapphire/Fe	3.04	1.97	N/A

[a]The Raman spectra were acquired from the base of the SWNT carpets after liftoff. N/A = not available.

and sputtered/Fe. On the other hand, the annealed e-beam/Fe sample is characterized by severe Ostwald ripening while the ALD/Fe sample is characterized by the lowest particle number density. The inset histograms of particle size distributions obtained using ImageJ[32] (Figure 5) show size range and number density. The particle number densities (N) in a 100 × 100 nm^2 area decreases in the order: e-beam/Fe (296) > sputtered/Fe (235) > ALD/Fe (175) > annealed e-beam/Fe (149). This result further supports our hypothesis that catalytic activity and lifetime are enhanced when Ostwald ripening is inhibited.

XPS depth profile analysis was carried out on the exposed catalysts after carpet growth for 15 min. The carpet removal procedure was carried out as described previously.[7,33] Figure 6 shows the integrated peak area ratios of Fe $2p_{3/2}$ and Al 2p as a function of sputtering time for the different catalyst samples. This analysis enabled us to probe the degree of inward diffusion of Fe in the alumina supports. Generally, as penetration depth increases, there is an initial increase of the Fe $2p_{3/2}$:Al 2p peak ratio for all the samples except sapphire/Fe, accompanied by a steady decrease in the ratio. The former increase in the ratio observed may be due to the selective coverage of the Fe particles by carbon materials. Since graphitic layers that encapsulate catalyst particles are robust,[34] it is possible that our carpet lift-off process did not remove all the carbon coating on the catalysts especially for sputtered/Fe and e-beam/Fe that are characterized by tall and highly dense SWNT carpets. It can be deduced from the profiles that the inward diffusion of Fe in alumina increases in the following order: sapphire/Fe < annealed e-beam/Fe < ALD/Fe < sputtered/Fe < e-beam/Fe. The evolution of Fe:Al for e-beam/Fe and sputtered/Fe is similar beyond a depth of 3 nm. However, below a depth of 3 nm, the atomistic subsurface diffusion rate of Fe for sputtered/Fe is intermediate between e-beam/Fe and ALD/Fe. Since sputtered/Fe is the best catalyst in this work, this result suggests that mild inward diffusion of Fe may be beneficial for high catalyst lifetime and activity.

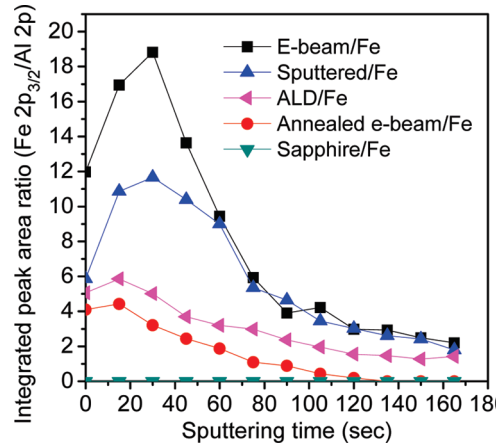

Figure 6. XPS depth profiles showing the degree of inward diffusion of Fe into the alumina support for e-beam/Fe, sputtered/Fe, ALD/Fe, annealed e-beam/Fe, and sapphire/Fe after exposure to SWNT carpet growth conditions for 15 min. The catalyst evolution is analyzed on the basis of the ratio of the integrated peak areas of Fe $2p_{3/2}$ and Al 2p as a function of sputtering time. The inward diffusion of Fe in alumina increases in the following order: sapphire/Fe < annealed/Fe < ALD/Fe < sputtered/Fe < e-beam/Fe.

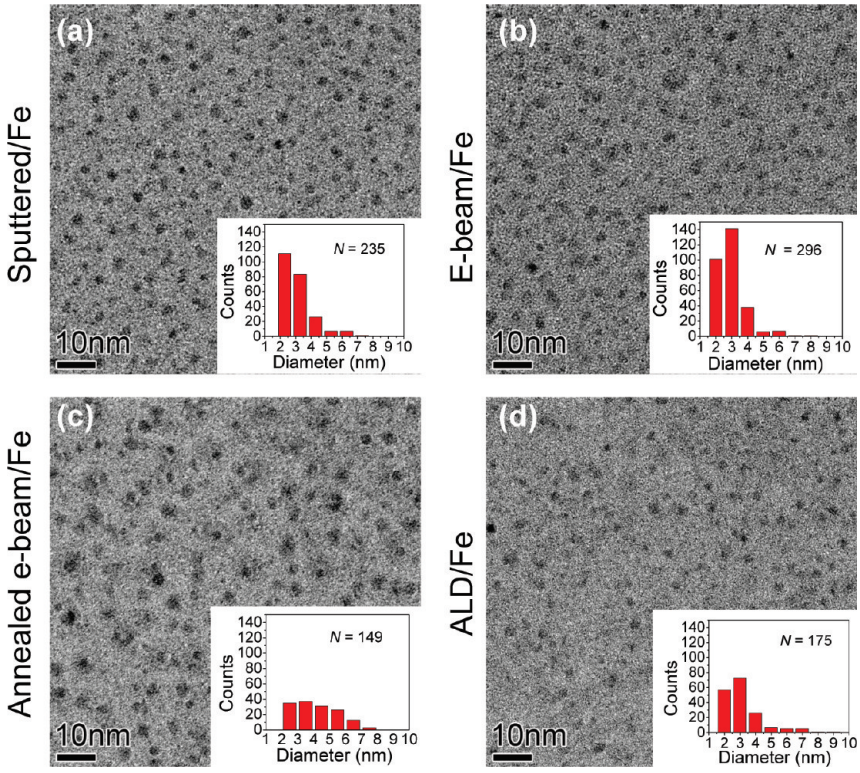

Figure 5. Plan-view TEM images of catalyst nanoparticles formed on (a) sputtered/Fe, (b) e-beam/Fe, (c) annealed e-beam/Fe, and (d) ALD/Fe after exposure to growth conditions in the absence of C_2H_2 for 15 min. All the scale bars are 10 nm, and all the panels have inset histograms showing particle size distributions, and the total number of particles (N) in a 100 × 100 nm^2 area. Sputtered/Fe and e-beam/Fe have higher number density than annealed e-beam/Fe and ALD/Fe; annealed e-beam/Fe is characterized by severe Ostwald ripening.

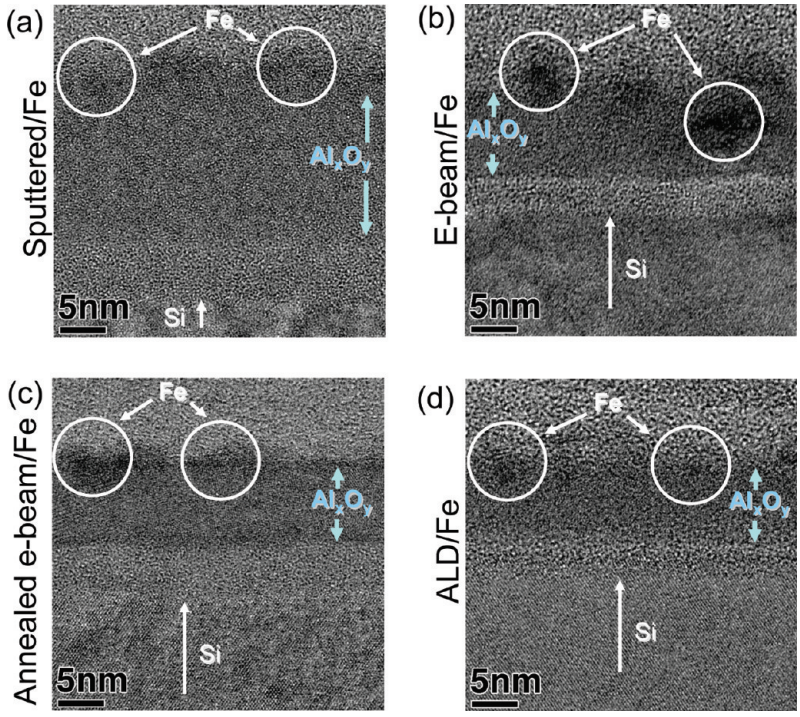

Figure 7. Cross-sectional TEM images of exposed (a) sputtered/Fe, (b) e-beam/Fe, (c) annealed e-beam/Fe, and (d) ALD/Fe catalysts after SWNT carpet growth for 15 min. The arrows indicate the Si and the alumina (Al_xO_y) layers, and the location of Fe. All the scale bars are 5 nm. There is high inward diffusion rate of Fe in e-beam/Fe as catalyst particles can be observed to have formed below the surface of the alumina layer. Catalyst particles are only observed on the surface for the other alumina-supported catalysts.

It should be noted that XPS depth profile analysis of the exposed catalyst samples after 5 min of carpet growth, within the time frame that the Ostwald ripening phenomenon dominates, reveal that the inward diffusion of Fe also occurs during this period (not shown). As a general feature, samples with high inward diffusion rate tend to have low Ostwald ripening rate. The cross-sectional TEM images of these samples presented in Figure 7 provide further proof of the high inward diffusion rate of Fe in e-beam/Fe as catalyst particles can be observed to have formed below the surface of the alumina layer. Although catalyst particles are only observed on the surface for the other alumina-supported catalysts, this result further substantiates that the inward diffusion rate is highest for e-beam/Fe.

To understand the role porosity plays in the inward diffusion of Fe and the catalytic activity and lifetime, we used variable angle spectroscopic ellipsometry (VASE) to characterize the optical properties of the pristine alumina films (without the Fe layer). The plots of refractive index as a function of wavelength for the as-received alumina supports (solid lines) and the thermally annealed supports (dashed lines) are presented in Figure 8. The dispersion in the refractive index for various porosities has been calculated using the Bruggeman effective medium approximation and indicated as arrows in Figure 8. Porosity and refractive index have an inverse relationship.[35] Thus porosity decreases in the following order: sapphire < ALD alumina < e-beamed alumina < sputtered alumina, and have the corresponding approximate porosities of 0%, 15%, 25%, and 36%. We observed that thermal treatment increases the density of the amorphous films (*i.e.*, decreases the porosity of the films) as observed in Figure 7c, especially for those with higher void fractions (sputter and e-beam deposited films). In general we observed ~5% change in the porosity before and after annealing except for the ALD film which had almost no change in the properties. The annealed e-beam deposited films showed lower void fractions, closer to dense sapphire than annealed alumina films deposited by ALD and sputtering. We should note that the sputtering process modified the Si substrate and damaged the alumina films, which made fitting of the data difficult. It is possible that the high catalytic activity of sputtered/Fe may also be due to the presence of this defective alumina that provides active sites for Fe catalyst. As a general feature, the Ostwald ripening rate appears to increase with decreasing porosity.

Figure 9 summarizes the effects of Ostwald ripening, subsurface diffusion, and the porosity of alumina supports on the catalytic activity for the different

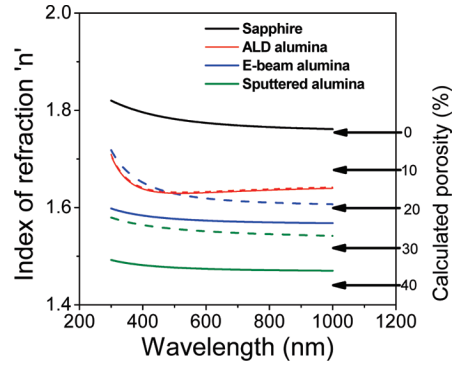

Figure 8. Index of refraction as a function of wavelength for the pristine alumina supports (solid lines) and after thermal annealing at 750 °C in air for 15 min (dashed lines). The curves were simulated to fit the curves using the Cauchy model. The arrows represent the dispersion in the refractive index for various porosities calculated using the Bruggeman effective medium approximation. The pristine alumina supports have different porosity and it increases with thermal annealing except for sapphire that was unaffected.

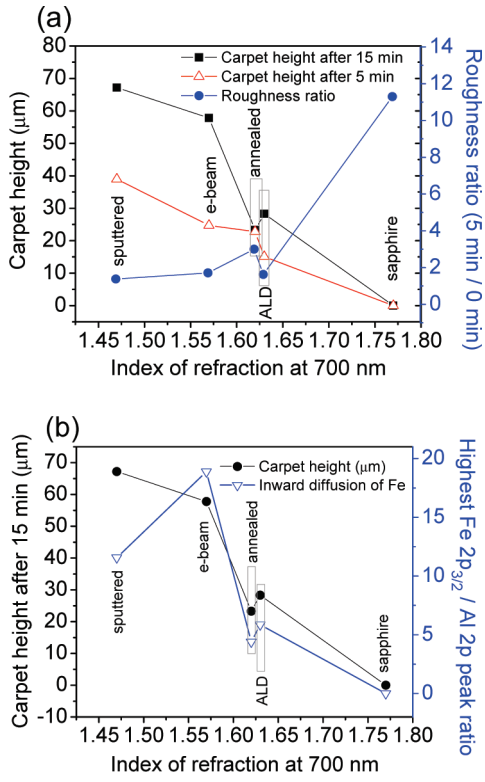

Figure 9. (a) Relationship between the index of refraction of the pristine alumina supports at 700 nm, roughness ratio of the alumina-supported catalysts at 5 and 0 min of thermal annealing, and SWNT carpet height after 15 min of growth for the alumina-supported catalysts. (b) Relationship between the index of refraction of the pristine alumina supports at 700 nm, carpet height after 15 min of growth for the alumina-supported catalysts, and the highest Fe $2p_{3/2}$/Al 2p ratio obtained from XPS depth profile analysis. The "annealed" represents thermally annealed alumina deposited by e-beam.

samples. The ratio of the average surface roughness of samples annealed for 5 and 0 min obtained from the AFM data (Figure 2) has been used to estimate the change in mean catalyst height and as a proxy for the rate of Ostwald ripening. Catalytic activity is high for samples with low Ostwald ripening rate and *vice versa*. We find that Ostwald ripening rate appear to increase with decreasing porosity of the alumina support. Sputtered/Fe and e-beam/Fe with high subsurface diffusion rate tend to have low Ostwald ripening rate while high Ostwald ripening rate is observed in annealed alumina/Fe with low subsurface diffusion rate. The longest carpets were grown from sputtered/Fe, which had a low Ostwald ripening rate, and subsurface diffusion rate that is intermediate between e-beam/Fe and ALD/Fe. Interestingly, the substrate for which complete growth termination occurred within the time range studied (15 min), that is, annealed e-beam/Fe has a Fe concentration profile that suggests that it may have been saturated with Fe through the thickness.

In summary, we have demonstrated that the activity and lifetime of Fe catalyst during water-assisted growth of SWNT carpets depends strongly on the porosity of alumina support. The catalytic activity increases in the following order: sapphire/Fe $<$ annealed e-beam/Fe $<$ ALD/Fe $<$ e-beam/Fe $<$ sputtered/Fe. A strong dependence of the dynamic evolution of Fe catalysts on the porosity of alumina support has been demonstrated. Catalyst samples with high inward diffusion rate such as sputtered/Fe and e-beam/Fe tend to have low Ostwald ripening rate. On the other hand, when the rate of inward diffusion is low, as observed in annealed e-beam/Fe and ALD/Fe, or nonexistent as in sapphire/Fe, the Ostwald ripening rate is higher. Also, catalytic activity increases with increasing porosity while Ostwald ripening rate appears to increase with decreasing porosity; the quality of CNTs increases with decreasing Ostwald ripening rate. Our work reveals that SWNT carpet growth is maximized by very low Ostwald ripening rates, mild subsurface diffusion rates, as well as high porosity of the alumina support, as observed in the sputtered/Fe catalyst. The complex interplay between Ostwald ripening, subsurface diffusion, and porosity of the alumina supports may account for the observed difference in catalyst lifetime and activity. Our data does not eliminate the possibility of variations in the stoichiometry of Al_xO_y contributing to the catalytic behavior. These results benefit ongoing efforts aimed at rational design of immortal catalysts for controlled and enhanced SWNT carpet growth.

EXPERIMENTAL SECTION

The catalyst consisted of a 0.5 nm thick Fe film deposited by e-beam evaporation on different types of alumina films supported on p-type Si (100) wafers. The nominally 10 nm thick alumina films were deposited by different techniques: atomic layer deposition (ALD), e-beam evaporation, and magnetron sputtering. Also used as catalyst supports were c-cut single crystal sapphire substrates [0001], and an alumina film deposited by e-beam evaporation followed by thermal anneal at 800 °C for 30 min, prior to Fe deposition. E-beam deposition of Fe and alumina films were conducted at room temperature; the chamber pressures were 7.5×10^{-7} and 1.5×10^{-6} Torr, respectively, while the deposition rate of Fe and alumina were 0.5 and 2 Å /sec, respectively. The deposition of alumina films by magnetron sputtering was conducted under 14 mTorr of Ar pressure with RF 160 W at room temperature; the deposition rate was ~3 Å/min. In the case of ALD, alumina films were deposited in N_2 ambient at 300 °C with a background pressure of $\sim 1 \times 10^{-3}$ Torr at a rate of 0.9 Å/cycle; the precursor used was $Al(CH_3)_3$.

In total, there were five catalyst configurations: (a) Fe supported on sapphire (sapphire/Fe), (b) Fe supported on sputter-deposited alumina (sputtered/Fe), (c) Fe supported on e-beam deposited alumina (e-beam/Fe), (d) Fe supported on thermally annealed alumina deposited by e-beam (annealed e-beam/Fe), and (e) Fe supported on alumina deposited by ALD (ALD/Fe). Since the stoichiometry of the amorphous alumina films is not known, "alumina" or "Al_xO_y" is used.

A detailed description of the CVD chamber and the growth conditions for SWNT carpet is given elsewhere.[36,37] The furnace was preheated to 750 °C, and the samples were rapidly inserted

into the furnace while the hot filament was energized. The pressure of the chamber was kept at 1.4 Torr. The respective flow rates were 400 sccm (standard cubic centimeters per minute) H_2, 2 sccm C_2H_2, and 2 sccm H_2O. The catalyst samples were exposed to atomic hydrogen generated by a hot filament for 30 s in order to rapidly reduce the metal-oxide catalyst particles. In addition, the samples were subjected to carpet growth environment in the presence of C_2H_2 for 1.5, 5, and 15 min. Following growth, the SWNT carpets were removed by a procedure described in ref 7. In brief, it involved an O_2 etch at 600 °C in air for 3 min to remove amorphous carbons at the SWNT/catalyst interface, and liftoff of the carpets with clear tape. Thermal annealing experiments were also performed for the same duration in the absence of C_2H_2,

AFM characterization of the catalyst substrates was carried out with a Digital Instrument Nanoscope IIIa system operating in the tapping mode with a scan rate of 2 Hz using Si_3N_4 tip cantilevers with a tip curvature radius of less than 10 nm. The cantilever oscillation frequency was set ~312 kHz. The height, amplitude, and phase data were acquired simultaneously for a scan size of 1×1 μm^2. The images acquired were flattened to remove any tilt in the image, and the statistical roughness was performed at the same scale of 1 μm using the WSxM 5.0 software.[31] In all measurements, nanoparticle heights as opposed to widths were measured because heights are unaffected by the variations in the tip radius, and the minimum cutoff particle height used for analysis was 0.6 nm.

The microstructure of the various types of alumina-supported Fe catalysts was studied using a field-emission transmission electron microscope/scanning transmission electron microscope (S/TEM) (80−300 Titan) from FEI Corporation. TEM sample preparation followed the procedure described elsewhere.[20] The growth products on the different alumina-supported catalysts after 1.5, 5, and 15 min were further characterized by Raman spectroscopy using a laser excitation wavelength of 633 nm. Raman spectra were obtained by removing the as-grown SWNT carpets from the substrate and focusing the laser spot on the bottom part of the carpets, which is at the interface with the Fe catalyst. Following subtraction of noise the ratios of the maximum G-band intensity (~1591 cm^{-1}) to that of the D-band (~1312 cm^{-1}) were determined.

X-ray photoelectron spectroscopy (XPS) sputter depth profile analysis was carried out on the alumina/Fe samples exposed to carpet growth for 15 min to probe the inward diffusion of Fe in the different types of alumina. The Surface Science Instruments (SSI) M-probe XPS is equipped with an Al Kα X-ray source operated at a base pressure of approximately 4.0×10^{-7} Pa. Spectra were analyzed using CASA XPS software, which has built-in corrections for spectrometer sensitivity factors for the SSI M-probe XPS. Fe 2p, C 1s, and Al 2p peak areas were measured using a Shirley background subtraction routine in order to compute the evolution of the Fe:Al ratio. The samples were sputtered for cycles of 5 s using Ar^+ with kinetic energy of 1 keV. The etching rate was calibrated using a SiO_2 film, and each sputtering cycle is estimated to produce a removal depth of ~0.5 nm except in the case of sapphire. A total of 20 cycles were performed.

Variable angle spectroscopic ellipsometry (VASE) was performed on the various alumina films before and after annealing to observe changes in refractive index which will allow us to infer changes in the density of the films. The data was collected and analyzed using a JA Woollam ellipsometer in the spectral range from 1.24 to 4.13 eV. A generic model was used with the following layer scheme: surface roughness/ema (Al_2O_3 and % void)/SiO_2/Si. Both the anneal and unannealed samples were fit simultaneously with the void fraction in the thermally annealed sample set to 0% and the unannealed sample's void fraction was allowed to vary to obtain the best fit. The overall alumina film refractive index was fit using a Cauchy layer with an Urbach tail, which has the assumed spectral dependence in eq 1, where *A*, *B*, and *C* are material dependent constants obtained through curve fitting, λ is the wavelength, and *n* is the index of refraction. In eq 2, κ is the extinction coefficient, γ is a fitting parameter that represents the band edge for the absorption process, β is a factor describing the rate at which the absorption decrease away from the edge, and α is a factor related to the strength of the absorption.

$$n = A + \frac{B}{\lambda^2} + \frac{C}{\lambda^4} \quad (1)$$

$$k = \alpha \exp\left(\beta 12400\left(\frac{1}{\lambda} - \frac{1}{\gamma}\right)\right) \quad (2)$$

A Bruggeman effective medium approximation was used to simulate the properties and the porosity changes in the alumina films. A SiO_2 layer thick was put in which corresponds to the thickness we typically observe on bare Si substrates. We did not let this vary because strong coupling existed between the SiO_2 thickness and the various other layers in the model.

Acknowledgment. This research is supported by the Air Force Office of Scientific Research (AFOSR) and Air Force Research Laboratory, Materials and Manufacturing Directorate. We thank Prof. T. D. Sands for helpful discussions, Dr. E. Shin for conducting alumina film deposition by magnetron sputtering, Prof. D. Natelson for use of e-beam evaporator, and Prof. P. Ye and his group for alumina film deposition by ALD. Special thanks to Dr. R. Rao and Prof. P.T. Murray for discussions.

Supporting Information Available: FESEM images of the side of the SWNT carpets, Raman spectra of the SWNT carpets, and profiles of the surface topography of the different alumina-supported catalysts after exposure to growth conditions. This material is available free of charge *via* the Internet at http://pubs.acs.org.

REFERENCES AND NOTES

1. Niu, C. M.; Sichel, E. K.; Hoch, R.; Moy, D.; Tennent, H. High Power Electrochemical Capacitors Based on Carbon Nanotube Electrodes. *Appl. Phys. Lett.* **1997**, *70*, 1480–1482.
2. Qu, L.; Dai, L. Gecko-Foot-Mimetic Aligned Single-Walled Carbon Nanotube Dry Adhesive with Unique Electrical and Thermal Properties. *Adv. Mater.* **2007**, *19*, 3844–3849.
3. Hinds, B. J.; Chopra, N.; Rantell, T.; Andrews, R.; Gavalas, V.; Bachas, L. G. Aligned Multiwalled Carbon Nanotube Membranes. *Science* **2004**, *303*, 62–65.
4. Coleman, J. N.; Khan, U.; Gun'ko, Y. K. Mechanical Reinforcement of Polymers Using Carbon Nanotubes. *Adv. Mater.* **2006**, *18*, 689–706.
5. Chen, J.; Liu, Y.; Minett, A. I.; Lynam, C.; Wang, J.; Wallace, G. G. Flexible, Aligned Carbon Nanotube/Conducting Polymer Electrodes for a Lithium-Ion Battery. *Chem. Mater.* **2007**, *19*, 3595–3597.
6. Hata, K.; Futaba, D. N.; Mizuno, K.; Namai, T.; Yumura, M.; Iijima, S. Water-Assisted Highly Efficient Synthesis of Impurity-Free Single-Walled Carbon Nanotubes. *Science* **2004**, *306*, 1362–1364.
7. Pint, C. L.; Xu, Y.-Q.; Pasquali, M.; Hauge, R. H. Formation of Highly Dense Aligned Ribbons and Transparent Films of Single-Walled Carbon Nanotubes Directly from Carpets. *ACS Nano* **2008**, *2*, 1871–1878.
8. Li, Q.; Zhang, X.; DePaula, R. F.; Zheng, L.; Zhao, Y.; Stan, L.; Holesinger, T. G.; Arendt, P. N.; Peterson, D. E.; Zhu, Y. T. Sustained Growth of Ultralong Carbon Nanotube Arrays for Fiber Spinning. *Adv. Mater.* **2006**, *18*, 3160–3163.
9. Murakami, Y.; Chiashi, S.; Miyauchi, Y.; Hu, M.; Ogura, M.; Okubo, T; Maruyama, S. Growth of vertically aligned single-walled carbon nanotube films on quartz substrates and their optical anisotropy. *Chem. Phys. Lett.* **2004**, *385*, 298–303.
10. Vander Wal, R. L.; Ticich, T. M.; Curtis, V. E. Substrate-Support Interactions in Metal-Catalyzed Carbon Nanofiber Growth. *Carbon* **2001**, *39*, 2277–2289.
11. Wang, B.; Yang, Y.; Li, L. -J.; Chen, Y. Effect of Different Catalyst Supports on the (*n*,*m*) Selective Growth of Single-Walled Carbon Nanotube from Co−Mo Catalyst. *J. Mater. Sci.* **2009**, *44*, 3285–3295.
12. Mattevi, C.; Wirth, C. T.; Hofmann, S; Blume, R.; Cantoro, M.; Ducati, C.; Cepek, C.; Knop-Gericke, A.; Milne, S.; Castellarin-Cudia, C.; *et al. In-Situ* X-ray Photoelectron Study of Catalyst-Support Interactions and Growth of

Carbon Nanotube Forests. *J. Phys. Chem C* **2008**, *112*, 12207–12213.
13. De los Arcos, T.; Garnier, M. G.; Oelhafen, P.; Mathys, D.; Seo, J. W.; Domingo, C.; García-Ramos, J. V. Sánchez-Cortés. Strong Influence of Buffer Layer Type on Carbon Nanotube Characteristics. *Carbon* **2004**, *42*, 187–190.
14. Han, S.; Yu, T.; Park, J.; Koo, B.; Joo, J.; Hyeon, T. Diameter-Controlled Synthesis of Discrete and Uniform-Sized Single-Walled Carbon Nanotubes Using Dispersed Iron Oxide Nanoparticles Embedded in Zirconia Nanoparticle Arrays as Catalysts. *J. Phys. Chem. B* **2004**, *108*, 8091–8095.
15. De los Arcos, T.; Garnier, M. G.; Seo, J. W.; Oelhafen, P.; Thommen, V.; Mathys, D. The Influence of Catalyst Chemical State and Morphology on Carbon Nanotube Growth. *J. Phys. Chem. B* **2004**, *108*, 7728–7734.
16. Bare, S. R.; Strongin, D. R.; Somorjai, G. A. Ammonia Synthesis over Iron Single-Crystal Catalysts: The Effects of Alumina and Potassium. *J. Phys. Chem.* **1986**, *90*, 4726–4729.
17. Ciuparu, D.; Chen, Y.; Lim, S.; Yang, Y.; Haller, G. L.; Pfefferle, L. Mechanism of Cobalt Cluster Size Control in Co-MCM-41 during Single-Wall Carbon Nanotube Synthesis by CO Disproportionation. *J. Phys. Chem. B* **2004**, *108*, 15565.
18. Ciuparu, D.; Haider, P.; Fernández-García, M.; Chen, Y.; Lim, S.; Haller, G. L.; Pfefferle, L. X-ray Absorption Spectroscopic Investigation of Partially Reduced Cobalt Species in Co-MCM-41 Catalysts during Synthesis of Single-Wall Carbon Nanotubes. *J. Phys. Chem. B* **2005**, *109*, 16332–16339.
19. Amama, P. B.; Pint, C. L.; McJilton, L.; Kim, S. M.; Stach, E. A.; Murray, P. T.; Hauge, R. H.; Maruyama, B. Role of Water in Supergrowth of Single-Walled Carbon Nanotube Carpets. *Nano Lett.* **2009**, *9*, 44–49.
20. Kim, S. M.; Pint, C. L.; Amama, P. B; Zakharov, D. N.; Hauge, R. H.; Maruyama, B.; Stach, E. A.; Dynamic Catalyst Evolution Leads to Carbon Nanotube Growth Termination. Unpublished work.
21. Somorjai, G. A. *Introduction to Surface Chemistry and Catalysis*; Wiley: New York, 1994; pp 442−480.
22. Pint, C. L.; Pheasant, S. T.; Pasquali, M.; Coulter, K. E.; Schmidt, H. K.; Hauge, R. H. Synthesis of High Aspect-Ratio Carbon Nanotube "Flying Carpets" from Nanostructured Flake Substrates. *Nano Lett.* **2008**, *8*, 1879–1883.
23. Meshot, E. R.; Hart, A. J. Abrupt Self-Termination of Vertically Aligned Carbon Nanotube Growth. *Appl. Phys. Lett.* **2008**, *92*, 113107–113109.
24. Bedewy, M.; Meshot, E. R.; Guo, H.; Verploegen, E. A.; Lu, W.; Hart, A. J. Collective Mechanism for the Evolution and Self-Termination of Vertically Aligned Carbon Nanotube Growth. *J. Phys. Chem.* **2009**, *113*, 20576–20582.
25. Li, Q.; Zhang, X.; DePaula, R. F.; Zheng, L.; Zhao, Y.; Stan, L.; Holesinger, T. G.; Arendt, P. N.; Peterson, D. E.; Zhu, Y. T. Sustained Growth of Ultralong Carbon Nanotube Arrays for Fiber Spinning. *Adv. Mater.* **2006**, *18*, 3160–3163.
26. Voorhees, P. W. The Theory of Ostwald Ripening. *J. Stat. Phys.* **1985**, *38*, 231–252.
27. Quintana, C.; Menendez, J. L.; Huttel, Y.; Lancin, M.; Navano, E.; Cebollada, A. Structural Charcterization of Fe (110) Islands Grown on α-Al_2O_3(0001). *Thin Solid Films* **2003**, *434*, 228–238.
28. Vitos, L.; Ruban, A. V.; Skriver, H. L.; Kollár, J. The Surface Energy of Metals. *Surf. Sci.* **1998**, *411*, 186–202.
29. Zaitsev, B. N.; Baklanova, N. I.; Zima, T. M. Atomic Force Microscopy Study of Surface-Modified Carbon Fibers. *Inorg. Mater.* **2008**, *44*, 592–597.
30. Paik, P.; Kar, K. K. Surface Roughness and Morphology of Polypropylene Nanospheres: Effects of Particle Size. *Surf. Eng.* **2008**, *24*, 341–349.
31. Horcas, I.; Fernández, R.; Gómez-Rodríguez, J. M.; Colchero, J.; Gómez-Herrero, J.; Baro, A. M. WSXM: A Software for Scanning Probe Microscopy and a Tool for Nanotechnology. *Rev. Sci. Instrum.* **2007**, *78*, 013705.
32. Rasband, W. S. *ImageJ*;U.S. National Institute of Health: Bethesda, Maryland, 1997, http://rsb.info.nih.gov/ij/.
33. Pint, C. L.; Kim, S. M.; Stach, E. A.; Hauge, R. H. Rapid and Scalable Reduction of Dense Surface-Supported Metal-Oxide Catalyst with Hydrazine Vapor. *ACS Nano* **2009**, *3*, 1897–1905.
34. Zhou, W.; Ooi, Y. H.; Russo, R.; Papanek, P.; Luzzi, D. E.; Fischer, J. E.; Bronikowski, M. J.; Willis, P. A.; Smalley, R. E. Structural Characterization and Diameter-Dependent Oxidative Stability of Single Wall Carbon Nanotubes Synthesized by the Catalytic Decomposition of CO. *Chem. Phys. Lett.* **2001**, *350*, 6–14.
35. Reisse, G.; weissmantel, S.; Keiper, B.; Steiger, B.; Johansen, H.; Martini, T.; Scholz, R. Influence of Ion Bombardment on the Refractive Index of Laser Pulse Deposited Oxide Films. *Appl. Surf. Sci.* **1995**, *86*, 107–113.
36. Pint, C. L.; Pheasant, S. T.; Para-Vasquez, A. N. G.; Horton, C.; Xu, Y.; Hauge, R. H. Investigation of Optimal Parameters for Oxide-Assisted Growth of Vertically Aligned Single-Walled Carbon Nanotubes. *J. Phys. Chem. C* **2009**, *113*, 4125–4133.
37. Pint, C. L.; Nicholas, N.; Pheasant, S. T.; Duque, J. G.; Parra-Vasquez, A. N. G.; Eres, G.; Pasquali, M.; Hauge, R. H. Temperature and Gas Pressure Effects in Vertically Aligned Carbon Nanotube Growth from Fe−Mo Catalyst. *J. Phys. Chem. C* **2008**, *112*, 14041–14051.